Transformation of taxol-stabilized microtubules into inverted tubulin tubules triggered by a tubulin conformation switch

Miguel A. Ojeda-Lopez[1][†][‡], Daniel J. Needleman[1][†][‡], Chaeyeon Song[2][‡], Avi Ginsburg[3], Phillip A. Kohl[4], Youli Li[4], Herbert P. Miller[5], Leslie Wilson[5], Uri Raviv[3], Myung Chul Choi[2] and Cyrus R. Safinya[1]*

Bundles of taxol-stabilized microtubules (MTs)—hollow tubules comprised of assembled αβ-tubulin heterodimers—spontaneously assemble above a critical concentration of tetravalent spermine and are stable over long times at room temperature. Here we report that at concentrations of spermine several-fold higher the MT bundles (B_{MT}) quickly become unstable and undergo a shape transformation to bundles of inverted tubulin tubules (B_{ITT}), the outside surface of which corresponds to the inner surface of the B_{MT} tubules. Using transmission electron microscopy and synchrotron small-angle X-ray scattering, we quantitatively determined both the nature of the B_{MT}-to-B_{ITT} transformation pathway, which results from a spermine-triggered conformation switch from straight to curved in the constituent taxol-stabilized tubulin oligomers, and the structure of the B_{ITT} phase, which is formed of tubules of helical tubulin oligomers. Inverted tubulin tubules provide a platform for studies requiring exposure and availability of the inside, luminal surface of MTs to MT-targeted drugs and MT-associated proteins.

Proteins often undergo abrupt structural transitions, which enables their functions. These discrete conformational changes underlie the exquisite control and sensitivity of biological organisms. Examples include pH-sensitive flagella and molecular motor ATPases such as kinesin and myosin motors undergoing conformational changes with altered states leading to discriminating binding affinities for $ADP + P_i$ and ATP (refs 1,2). In contrast to the (switch like) discrete conformational states of proteins, many other biomacromolecules undergo continuous shape changes. For example, lipids may form spherical and cylindrical micelles, bilayers or other assemblies, as variations in their local environment (pH, ionic strength, addition of co-lipids) continuously change the lipid's shape[3–7].
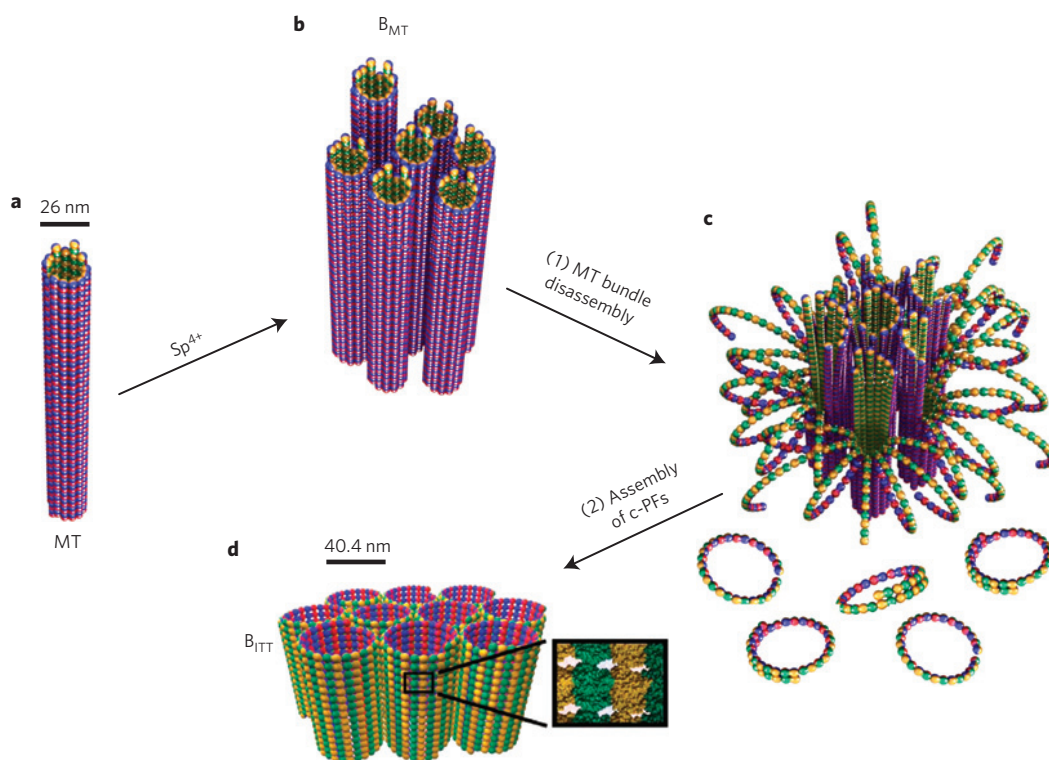
In our studies we used proteins, which harness the discrete shape-remodelling specificity used in biology, as self-assembling building blocks. These 'genetically pre-programmed' nanomaterials were found to be susceptible to molecularly triggered disassembly and the simultaneous reassembly and emergence of a new structure. This paradigm for self-assembly is distinct from those employed previously, where the complementary binding (that is, recognition specificity) present in proteins, DNA and RNA is used to construct specific contact between sub-units, allowing assembly into predictable yet relatively stable structures[8–11].

The building blocks in our study were αβ-tubulin heterodimers, which exist in two distinct conformations, with the transition between these two states controlled by GTP hydrolysis[12–14]. Tubulin's distinct conformations underlie the broad range of cellular functions of tubulin and polymerized tubulin (that is, MTs), which include imparting cell shape, as tracks for organelle transport, and as building blocks of dynamical spindles[1,2]. Protofilaments (PFs)—head-to-tail assemblies of αβ-tubulin heterodimers—adapt straight and curved conformations for the GTP–tubulin and GDP–tubulin states, respectively. The assembled MT (Fig. 1a), consisting on average of 13 straight PFs, is stabilized by lateral PF–PF interactions. MT disassembly (for example, during dynamic instability) occurs when the layer of GTP-containing β-subunits at the MT growing end is lost, and when MTs depolymerize the PFs peel off as highly bent GDP–tubulin oligomers[12,15]. The cancer chemotherapy drug taxol maintains the straight conformation for GDP–PFs (post hydrolysis) on binding to the β-subunit facing the inner lumen[16–19]. Taxol stabilizes the straight conformation for GDP–PFs by raising the energy barrier and thus preventing the straight-to-curved transition over very long periods of time, of the order of many weeks to months (depending on the molar ratio of taxol to tubulin dimers)[20,21]. Indeed, elegant atomic force microscopy studies, at the single-PF level, of taxol-stabilized straight and ring-like GDP–PFs show that taxol slows down the straight-to-curved transition of GDP–PFs (ref. 20).

In a previous study it was found that taxol-stabilized MTs can be induced to assemble into hexagonally packed bundles,

Figure 1 | Schematic of a spermine (4+ or Sp^{4+})-induced inversion process from bundles of taxol-stabilized MTs (B$_{MT}$) to bundles of ITTs (B$_{ITT}$).
a,b, Taxol-stabilized MTs (**a**) may be induced to form MT bundles above a critical concentration of Sp^{4+} counterions (**b**). The bundles result from the nonspecific electrostatic attraction between spermine-coated MTs. **c,d**, For concentrations several times larger than the critical bundling concentration, a specific spermine-triggered straight-to-curved conformation transition in PFs leads to MT disassembly into c-PFs within the bundles (**c**). Concurrent to MT disassembly, spermine counterions induce nonspecific assembly of c-PFs into the B$_{ITT}$ phase (**d**). Both phases are hierarchically ordered, liquid-crystalline nanotubes, but the tubes are inverted: the tubulin surface, which is on the inside of the tubes in the B$_{MT}$ phase, is on the outside in the B$_{ITT}$ phase.

the B$_{MT}$ phase, above a critical concentration of tetravalent spermine (4+; Fig. 1b)[22]. The origin of the assembly lies in counterion-induced electrostatic attractions[23,24] between spermine-coated MTs (ref. 25). Spermine is a biological polyamine present at millimolar concentrations in eukaryotic cells, and, as an efficient counterion to anionic cytoskeletal filaments (for example, F-actin and MTs), may have a regulatory role on the architecture of cytoskeletal networks in cells[26].

Here, we find that whereas the spermine-induced MT bundled structure (Fig. 1b) is stable for long periods at concentrations just above the critical bundling concentration (C_c) at room temperature[22], at higher concentrations (several times C_c) spermine triggers bundle disassembly by inducing a straight-to-curved transition and the outwardly peeling of taxol-containing PFs within bundles (Fig. 1c). Concurrently, the presence of counterion spermine leads to assembly of curved PFs (c-PFs) into a tubular structure (Fig. 1d), which as transmission electron microscopy (TEM) shows, is distinct from tubules formed by GDP–PFs in the straight conformation. Furthermore, quantitative analysis of synchrotron small-angle X-ray scattering (SAXS) data reveals that the single-walled tubules consist of helical PFs, with the tubules ordered into hexagonal bundles. Thus, as TEM and SAXS show, PFs in the curved and straight conformations both form arrays of hollow nanometre-scale tubules, but because of the inside-out curving of PFs during the peeling process, the surface that is on the inside of the B$_{MT}$ tubes (Fig. 1b) is outside on the new array of tubules. We refer to this structure as a bundle phase of inverted tubulin tubules (B$_{ITT}$; Fig. 1d). Our discovery is consistent with the hypothesis that spermine controls the energy barrier between the straight and curved conformations of taxol-stabilized GDP–PFs; and as time-dependent SAXS shows spermine lowers the barrier with increasing concentrations.

Tubulin may be induced to form a variety of alternative structures in the presence of polycations and divalent cations[27–33]. Double-walled structures have been observed to result from tubulin in reassembly buffer (containing GTP) at 37 °C, which contains cationic DEAE-dextran[27,28,30] or a range of synthetic polycations[29]. TEM shows that the double-walled structure consists of tubulin rings wrapped around a MT core[27–30]. As more recent cryo-TEM studies have shown that tubulin rings have a natural inside-out curvature[12,15], it follows that the rings in the double-walled structures of the earlier work[27–30] also have the same orientation. A recent cryo-electron microscopy study of Mn^{2+}-induced assembly of GDP–tubulin at 37 °C has revealed the formation of a different type of double-layered tube, with PFs aligned approximately perpendicular to the tube axis for both layers[33]. Cryo-EM reconstruction at 1.2 nm resolution shows that the outer wall consists of a tight one-start helix of 32 tubulin monomers with an inside-out orientation of the PF. The orientation and helical nature of the outer wall of these double-walled tubes seem to be quite similar to the single-walled inverted tubulin tubules (ITTs) described here.

Here we show in some detail, using TEM and SAXS, the pathway of inversion of bundles of taxol-stabilized-MTs into bundles of single-walled tubules. The discovery of spermine-triggered depolymerization of MTs is highly surprising given the known stabilizing effects of taxol on MTs against a variety of destabilizing conditions including cold[16–19]. Furthermore, whereas the depolymerization of taxol-stabilized MTs seems to have specificity (for example, spermidine, a closely related oligoamine, does not depolymerize taxol-stabilized MTs on the timescale of 2–3 weeks), the formation of a variety of double-walled structures from
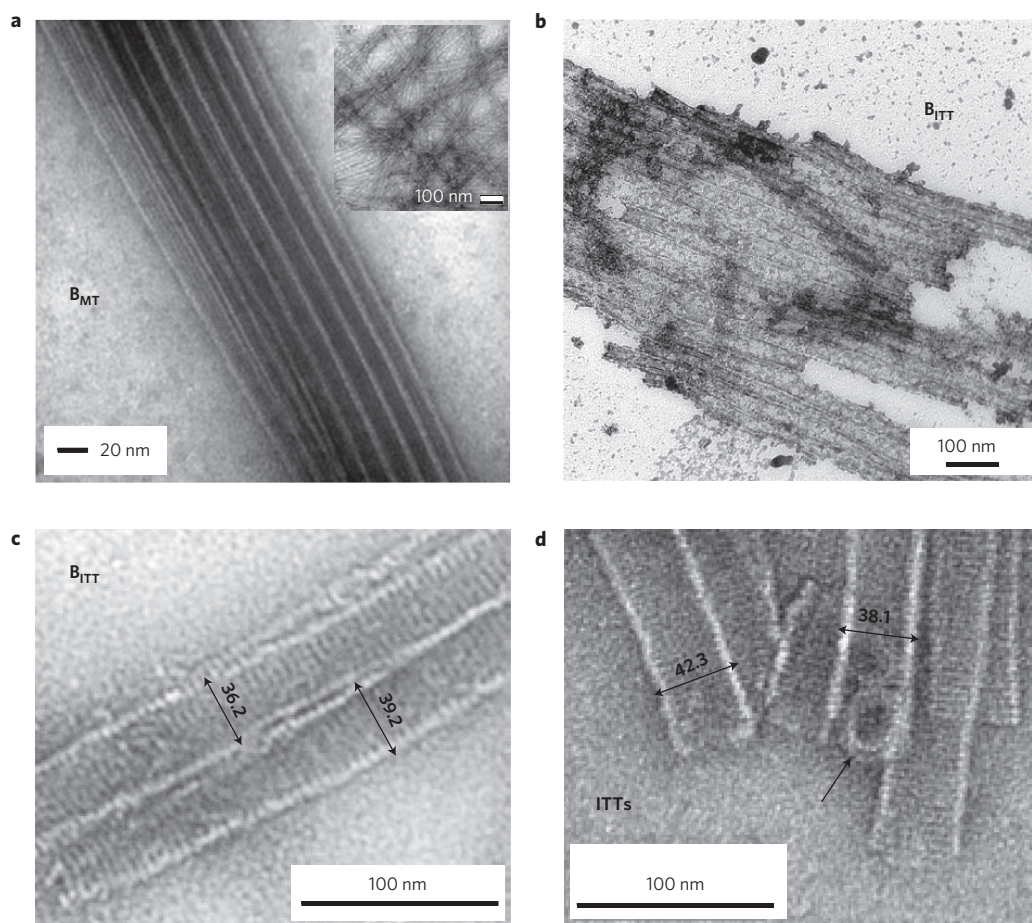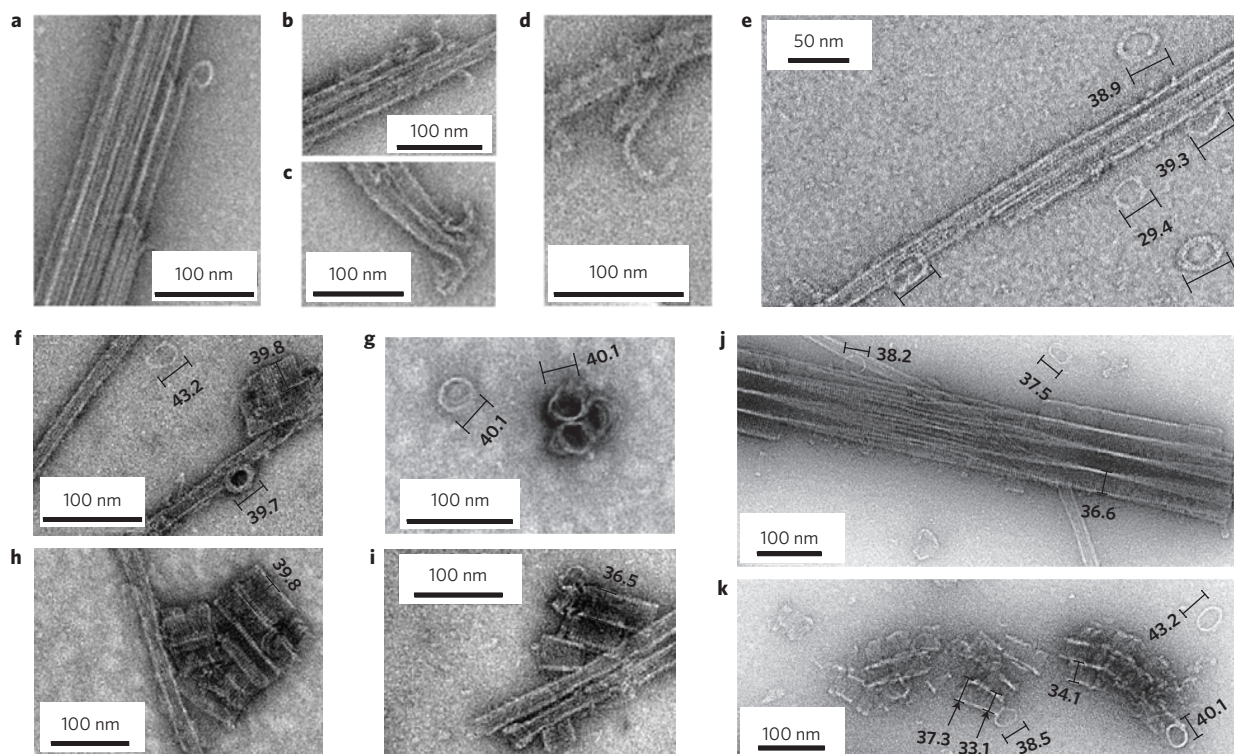
Figure 2 | TEM images of taxol-stabilized MT bundles (B_{MT}) and the new spermine-induced phase of bundles of ITTs (B_{ITT}). a, A typical TEM image of a taxol-stabilized MT bundle (10 mM spermine, room temperature) showing striations parallel to the cylinder axis due to the PFs. The bundle phase is dominant for less than 10 days. Inset: Taxol-stabilized MTs with straight PFs (18.18 μM tubulin, taxol/tubulin molar ratio of 0.55) at a lower magnification and in the absence of spermine. **b,c**, An example of a large bundle of ITTs (**b**, B_{ITT}) and a higher magnification of a smaller B_{ITT} (**c**) where PFs appear as striations perpendicular to the cylinder axis. The TEM images are for 25 mM spermine mixed with taxol-stabilized MTs and imaged after 10 days at room temperature. **d**, Example of the B_{ITT} phase formed 24 h after addition of 12.5 mM spermine at 4 °C. Arrow points to overlapping PF rings. In this sample preparation, a sucrose cushion to remove unpolymerized tubulin (which was used for TEM samples; **a–c**) was not employed and ITTs depicted here coexist with double-walled structures, shown in Supplementary Fig. 4 (see sample preparation details in Methods). All TEM images were for samples at a taxol/tubulin molar ratio of 0.55.

tubulin[27–30,33], mixed with a range of cationic macromolecules or divalent ions, seems to be nonspecific.

The transition from the B_{MT} to B_{ITT} phase is strongly temperature-dependent, varying between days to hours in going from room temperature to 0 °C with spermine concentrations in the millimolar range. A TEM micrograph of a relatively large bundle of taxol-stabilized MTs formed in the presence of 10 mM spermine (well above the critical bundling concentration C_c of 1.5 ± 1 mM) can be seen in Fig. 2a. For these preparations, the B_{MT} phase is the dominant component for less than 10 days at room temperature, after which coexistence with the new B_{ITT} phase is observed. At higher spermine concentrations (≥ 15 mM) at room temperature, the B_{MT} phase is progressively replaced by the new B_{ITT} phase after 10 days. A large bundle of the B_{ITT} phase 10 days after addition of 25 mM spermine to MTs at room temperature is shown in the TEM micrograph in Fig. 2b. A high-magnification example of a small bundle of the B_{ITT} phase prepared under the same conditions is shown in Fig. 2c. The transition from the B_{MT} phase to this new phase is observed to occur on much shorter timescales at 4 °C; Fig. 2d shows an example of the B_{ITT} phase 24 h after addition of spermine at a lower concentration of 12.5 mM. Whereas the columnar nature of the phase is evident, the observation

of striations perpendicular to the tube axis is striking (compare Fig. 2b–d with the MT bundle in Fig. 2a having PFs parallel to the tubular axis). As we describe below, SAXS data show that the striations comprising the ITT walls correspond to helical PFs.

To discover the transient structures, along the transition pathway from the B_{MT} to the B_{ITT} bundled phase, a series of samples at 12.5 mM spermine were maintained at 4 °C (in a water bath) and imaged at various times (30 min, 1, 2, 5, 19 h) to capture early, early-to-intermediate, intermediate, and late time frames in the structural evolution between the bundled states (Fig. 3a–k). At the very early stages of the transition from the B_{MT} phase (30 min post-addition of 12.5 mM spermine at 4 °C) with primarily MT bundles (B_{MT}) present, TEM shows the inside-out curling of PFs, often at the ends of the bundles and sometimes along the body of the bundle (Fig. 3a–d and Supplementary Fig. 1). The diameter of the 'pre-ring' curled PFs range from as small as ≈28 nm (Fig. 3a) to as large as ≈45.1 nm (Fig. 3d) and 49.8 nm (see Supplementary Fig. 1a–f for diameters of a collection of 'pre-ring' structures). Thus, although many initial curling PFs have a smaller diameter than the fully formed PF-rings observed at later times (discussed below), there are also examples of larger diameters. The large variation in the diameter at this 'pre-ring stage' may not be surprising because

Figure 3 | Time-dependent TEM of the pathway of inversion of taxol-stabilized MT bundles (B_{MT}) into bundles of ITTs (B_{ITT}) at 4 °C and 12.5 mM spermine. a–d, TEM images of early stages of MT bundle disassembly at 30 min showing the inside-out curling of PFs into 'pre-ring' structures with a large variation in their diameters (see Supplementary Fig. 1). This stage corresponds to Fig. 1c. **e**, Early-to-intermediate stage TEM images at 2 h show the presence of fully formed rings surrounding MT bundles, which dominate the phase at this early-to-intermediate stage where the inverted tubulin structure has not yet formed. TEM images at 1 h show similar structures. **f–i**, Intermediate-stage TEM images at 5 h showing short ITTs and ITT bundles (including an end view of an ITT trimer in **g**) co-existing with rings, MTs and MT bundles. **j**, Late-stage TEM image at 19 h show fully formed bundles of ITTs and few isolated MTs and rings. In the final stage, in the B_{ITT} phase, no remaining MTs (and extremely few rings) are found as seen in Fig. 2 both at room temperature (Fig. 2b,c) and at 4 °C 24 h post addition of 12.5 mM spermine (Fig. 2d). **k**, A TEM image of a different region of the same sample as in **j** at 19 h showing a rare region where short ITTs seem to be forming from the assembly of rings. The variation in the diameter of assembled rings is visible during ITT formation as discussed in the text. The rings in **e–k** have diameters that are approximately that of the ITTs. In the measurement of ring size, the longer axis was taken because tilts in the ring make it appear as elliptical, with the longer axis being a closer estimate of the true diameter. The sample preparations for TEM images (**b,c** at 30 min) and (**e–k** at 2, 5, 19 h) employed a sucrose cushion to remove unpolymerized tubulin after taxol-stabilization of MTs. The sucrose cushion was not employed for TEM samples (**a,d** at 30 min; see sample preparation details in Methods). All TEM images were for samples at a taxol/tubulin molar ratio of 0.55.

the curling PFs are highly dynamical and the TEM images capture a moment during the peeling process.

Figure 3e–k shows TEM images corresponding to later times along the transition at 4 °C. TEM images after 1 and 2 h were qualitatively similar where MT bundles are seen to coexist with fully formed rings with no hint of ITTs (Fig. 3e, early-to-intermediate stage TEM at 2 h). Figure 3f–i shows intermediate-stage TEM images of different regions of the same sample at 5 h, where one can now see emerging short ITTs and ITT bundles (including an end-view of an ITT trimer in Fig. 3g) coexisting with rings, MTs and MT bundles. Further along at 19 h, bundles of ITTs now dominate the structure at this late stage, and fully formed bundles of ITTs are seen to coexist with some rings, very few MTs and no MT bundles (Fig. 3j). It is interesting to note that whereas the micrograph in Fig. 3j shows a well-ordered bundle of ITTs, Fig. 3k shows a more rare region of the same sample at 19 h, where short emerging ITTs (with a few rings around them) seem to merge and interact laterally. The diameters of the rings seen in TEM images (Fig. 3e–k) are now seen to be comparable to the diameter of the ITTs (Figs 3f–k and 2c,d). A notable observation in the TEM of Fig. 3k is that one can see that the assembling rings along the tubes have highly non-uniform diameters (see, for example, arrows pointing to different diameters along the tube), which become more

uniform (Fig. 3j) once the ITTs are fully formed with the rings opening/fusing to form the helical PFs comprising the tubule wall (with the helical nature confirmed by SAXS). We do not expect the inside-out rings to further twist and expose another surface in the process of going from rings to the helical PFs, as this would result in a large elastic cost. Furthermore, the similarities in pitch and size between the single-walled tubule shown here and the outer layer of the previously observed double-layered tubule at 1.2 nm resolution[33] strongly suggest that the outer surface of the ITTs corresponds to the inner lumen of MTs.

Observations from TEM images covering the early to intermediate, late and final stages of conversion of the B_{MT} phase to the B_{ITT} phase indicate that the tubulin rings are the building blocks of the nascent ITTs. The formation of inside-out rings (Fig. 3e) after the initial curling of PFs (Fig. 3a–d) and before the emergence of B_{ITT} structures (Fig. 3f–i), and their near absence in the B_{ITT} phase (Fig. 2d after 24 h at 4 °C; see also the B_{ITT} phase TEM images at room temperature after 10 days in Fig. 2b,c), indicates that they have self-assembled in the presence of cationic spermine into the ITTs, with the outer surface corresponding to the inside luminal surface of the MTs.

To further show that the rings are the building blocks of the ITTs, we performed a comprehensive statistical analysis of
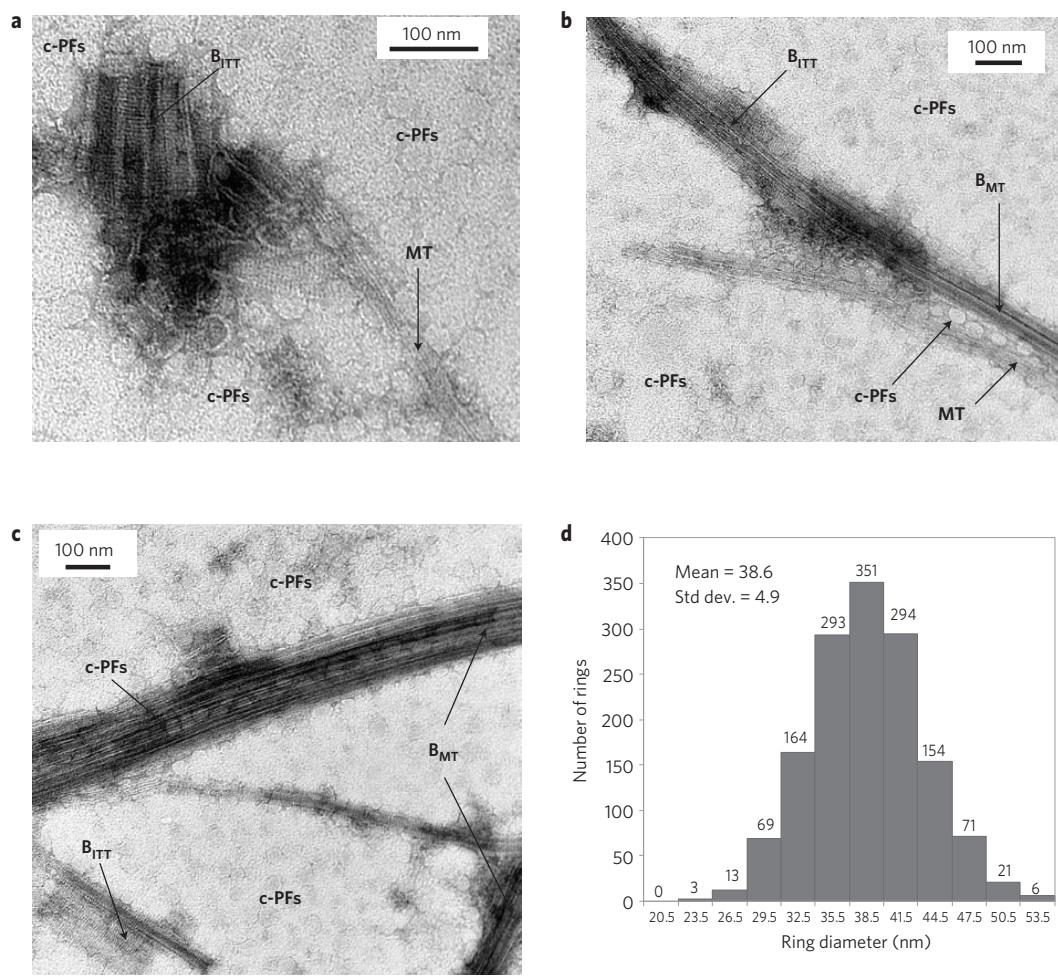
Figure 4 | Size distribution of ring-like PFs in the coexistence regime of disassembling MT bundles (B$_{MT}$) and assembling bundles of ITTs (B$_{ITT}$) from TEM. a–c, TEM images (15 min after addition of 15 mM spermine at 0 °C) show coexistence of B$_{MT}$ with short bundles of ITTs (B$_{ITT}$). Also seen is the proliferation of ring-like c-PFs, both in the vicinity of the bundled structures and within disassembling MT bundles (arrows pointing to c-PFs in **b,c**). **d**, Size distribution of 1,439 rings in a larger part of the sample surrounding the region shown in the TEM image in **a** (see Supplementary Fig. 2). The total number of rings in each bar (with a width of 3 nm) is indicated at the top of each bar. The mean size of 38.6 nm, with a standard deviation of 4.9 nm for the rings is consistent with the diameter of ITTs (≈40.4 nm) measured with SAXS of undistorted bundles of ITTs in solution. All TEM images were for samples at a taxol/tubulin molar ratio of 0.55.

the distribution of ring diameters in a TEM micrograph of disassembling MT bundles that showed a very large number of rings. Figure 4a–c shows micrographs of samples that already after 15 min at $T \approx 0\,°C$ (with 15 mM spermine immersed in ice) show an intermediate regime with coexistence of MT bundles and short ITT bundles together with an abundance of tubulin rings both surrounding and within the bundles (see, for example, arrow pointing to c-PFs in the depolymerizing MT bundle in Fig. 4b). Figure 4d shows a histogram (number of rings versus ring diameter) of 1,439 rings taken from a large area surrounding the region shown in Fig. 4a (see full-size TEM in Supplementary Fig. 2). The mean ring diameter is 38.6 nm, with a standard deviation of 4.9 nm. We now see that the mean diameter of the ITTs observed in the TEM images (Figs 2c,d and 3f–k) is within the measured standard deviation (±4.9 nm) of the mean diameter of the 1,439 rings. The size measurements from TEM agree well with the analysis of the X-ray SAXS data, which shows that the diameter of ITTs in solution (with no distortions) is on average 40.2 nm (the TEM data are for samples under vacuum, which invariably leads to some level of distortions).

To gain quantitative insight into the ångström-level structure of the ITTs and the kinetics of the structural evolution from the

B$_{MT}$ to the B$_{ITT}$ phase, we carried out a series of synchrotron SAXS studies of taxol-stabilized MTs at various spermine concentrations and over short and long times. The lower two profiles in Fig. 5a show synchrotron SAXS intensity as a function of the magnitude of the scattering wavevector q at room temperature for MTs and MT bundles (labelled B$_{MT}$) in the presence of 5 mM spermine 10 days after bundle formation. After background subtraction (Methods), the scattering from MTs can be quantitatively fitted to $|F_{MT}|^2 \propto |[\sin(q_z L/2)/q_\perp q_z][(R_{in}+w)J_1(q_\perp(R_{in}+w)) - R_{in}J_1(q_\perp R_{in})]|^2$, averaged over all orientations in q-space (Fig. 5b, MT, solid line through data, open circles). Here, F_{MT} is the X-ray form factor of a hollow cylinder with an inner radius $R_{in} = 80$ Å, a wall thickness $w = 49$ Å, and length much larger than R_{in} (over 1,000 nm; refs 21,22,34,35). $q_\perp, q_z$ are wavevectors perpendicular and parallel to the tubular axis, respectively, and J_1 is the Bessel function of order 1. The measured dimensions are consistent with high-resolution models of MTs with an average of 13 PFs (ref. 13).

The diffraction peaks of the B$_{MT}$ phase (Fig. 5a) can be indexed to MTs arranged on a hexagonal lattice with a centre-to-centre distance $a_H = 4\pi/\sqrt{3}q_{10}$. This results in diffraction peaks at q_{10}, $q_{11} = \sqrt{3}q_{10}$, $q_{21} = \sqrt{7}q_{10}$ and $q_{31} = \sqrt{13}q_{10}$. (The q_{20}, q_{30} and q_{22} peaks are close to the minima of the MT form factor and appear as
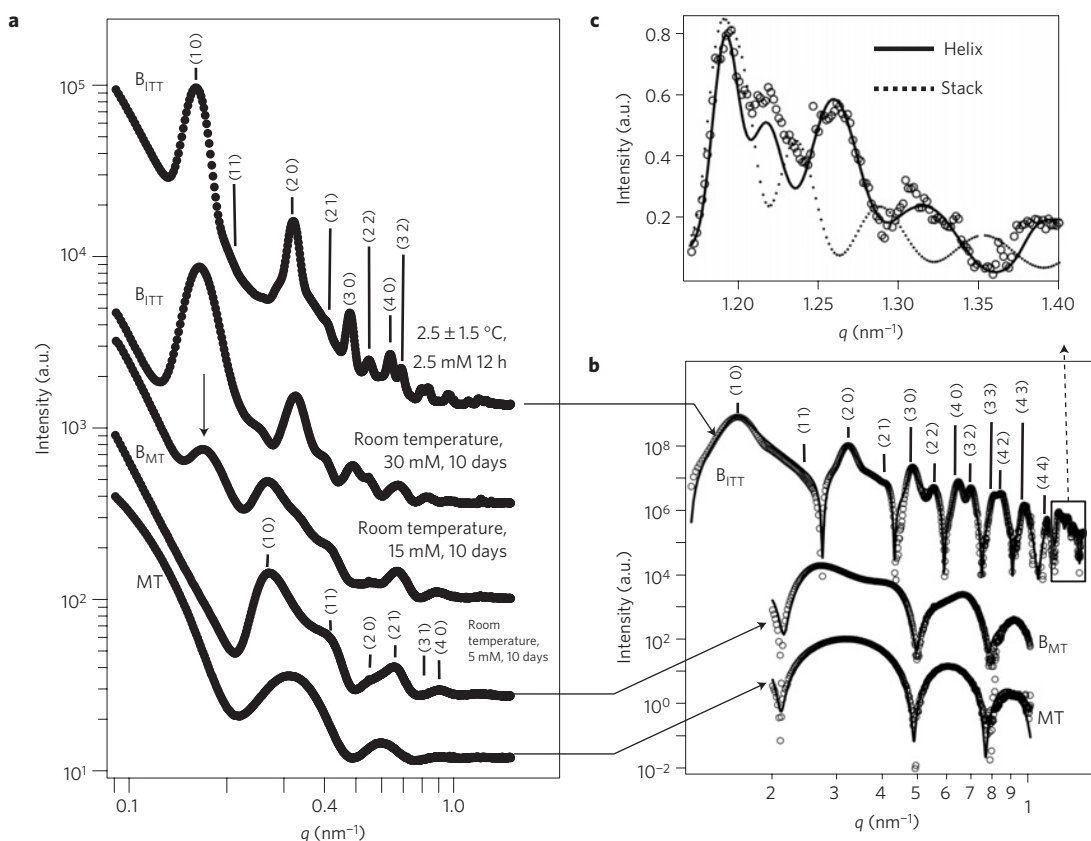
Figure 5 | Synchrotron SAXS data of taxol-stabilized MT bundles (B$_{MT}$) and bundles of ITTs (B$_{ITT}$). a, Bottom profile shows synchrotron SAXS data of taxol-stabilized MTs. The second to fourth profiles from the bottom are SAXS data from room-temperature samples taken 10 days after mixing increasing amounts of spermine with MTs: 5 mM spermine shows 2D hexagonal bundles of MTs (B$_{MT}$); 15 mM spermine shows coexistence of the B$_{MT}$ phase with the new phase of bundles of ITTs (B$_{ITT}$, arrow points to the first-order diffraction peak); and 30 mM spermine shows the B$_{ITT}$ phase. Top profile shows SAXS of the B$_{ITT}$ phase formed at ≈2.5±1.5 °C 12 h after placing MTs in the B$_{MT}$ phase, with 2.5 mM spermine. **b**, Three scattering profiles from **a** (bottom two and top curves) after background subtraction with fitted model scattering curves (solid lines) as described in the text. Twelve peaks of the B$_{ITT}$ phase can be indexed to a 2D hexagonal lattice. **c**, Expanded high q region showing comparison of scattering data with a model where the inverted tubulin columns consist of either helical PFs with a tight pitch (solid line, which fits the data well) or stacks of rings of c-PFs (dotted line, which does not fit the data). All samples were at a taxol/tubulin molar ratio of 0.55.

weak peaks.) The background-subtracted SAXS data for unoriented MT bundles (Fig. 5b, B$_{MT}$, open circles) are well fitted by the MT form factor multiplied by the structure factor and averaged over all orientations in q-space (Fig. 5b, B$_{MT}$, solid line). Following previous work, the structure-factor peaks at each reciprocal lattice vector $\mathbf{G}_{hk}$ were modelled as squared Lorentzians, $[A_{hk}/(\kappa^2 + (q_\perp - G_{hk})^2)]^2$, with G_{hk}, amplitude A_{hk} and a single peak width proportional to κ as fitting parameters[22]. The nonlinear least-squares fit of the model to the SAXS data gives $a_H = 28.7$ nm and $\kappa = 0.0041$ Å^{-1}, which leads to an average bundle width $L \approx 2(\pi\ln4)^{0.5}/\kappa = 101.3$ nm, corresponding to an average of ≈3.5 MTs (Methods).

For MT bundles at 15 mM spermine, the SAXS data after 10 days at room temperature (Fig. 5a) now show evidence of coexistence of the bundled B$_{MT}$ phase with the new B$_{ITT}$ phase (arrow points to the first-order diffraction peak of the B$_{ITT}$ phase). At 30 mM spermine, the entire sample is in the B$_{ITT}$ phase after 10 days at room temperature (Fig. 5a).

As mentioned earlier, the B$_{MT}$-to-B$_{ITT}$ structural transformation at a constant spermine concentration is observed to occur at a greatly increased rate with decreasing temperature. At 2.5 ±1.5 °C, MTs bundled with 2.5 mM spermine (where the B$_{MT}$ phase is stable for more than 10 days at room temperature) are observed to have undergone the transition to the B$_{ITT}$ phase after 12 h (Fig. 5a,b, top profiles). The data range from q values less than 0.1 nm^{-1} to a q of 1.4 nm^{-1}, covering length scales from greater than 62 to 4.5 nm.

For the low q range between 0.1 and 1.0 nm^{-1}, 12 Bragg peaks are clearly visible (Fig. 5b) and can be indexed to a two-dimensional (2D) hexagonal lattice.

A quantitative fit of the data to a model scattering curve after background subtraction (Fig. 5b, top profile, black line) shows that the B$_{ITT}$ phase consists of hexagonal bundles of helices. The model consisted of $|F_{\text{finite size helix}}|^2$ (where $F_{\text{finite size helix}}$ is the form factor of a finite-size helical tubulin oligomer) multiplied by a Lorentzian squared structure factor (as described for the B$_{MT}$ phase) and averaged over all orientations in q-space. For an infinitely long continuous helix oriented along the z-helical axis, F_{helix} is proportional to Bessel functions of order n, $J_n(q_\perp R)$, located on discrete layer lines at $q_z = 2\pi n/P$, where n is an integer, P is the helical pitch and R is the radius of the helix[36]. To take into account both the finite length of the helix and the thickness of tubulin we used:

$$|F_{\text{finite size helix}}|^2 \propto \sum_n |J_n(q_\perp R)|^2 \exp[-(q_z - 2\pi n/P)^2 L_z^2/4\pi]$$
$$\times \exp[-(q_\perp^2 + q_z^2)R_g^2/2] \qquad (1)$$

The first Gaussian function is Warren's approximation accounting for the finite length of the helix $L_z = NP$ (where N is the number of turns in the helix) and replaces the delta function peaks
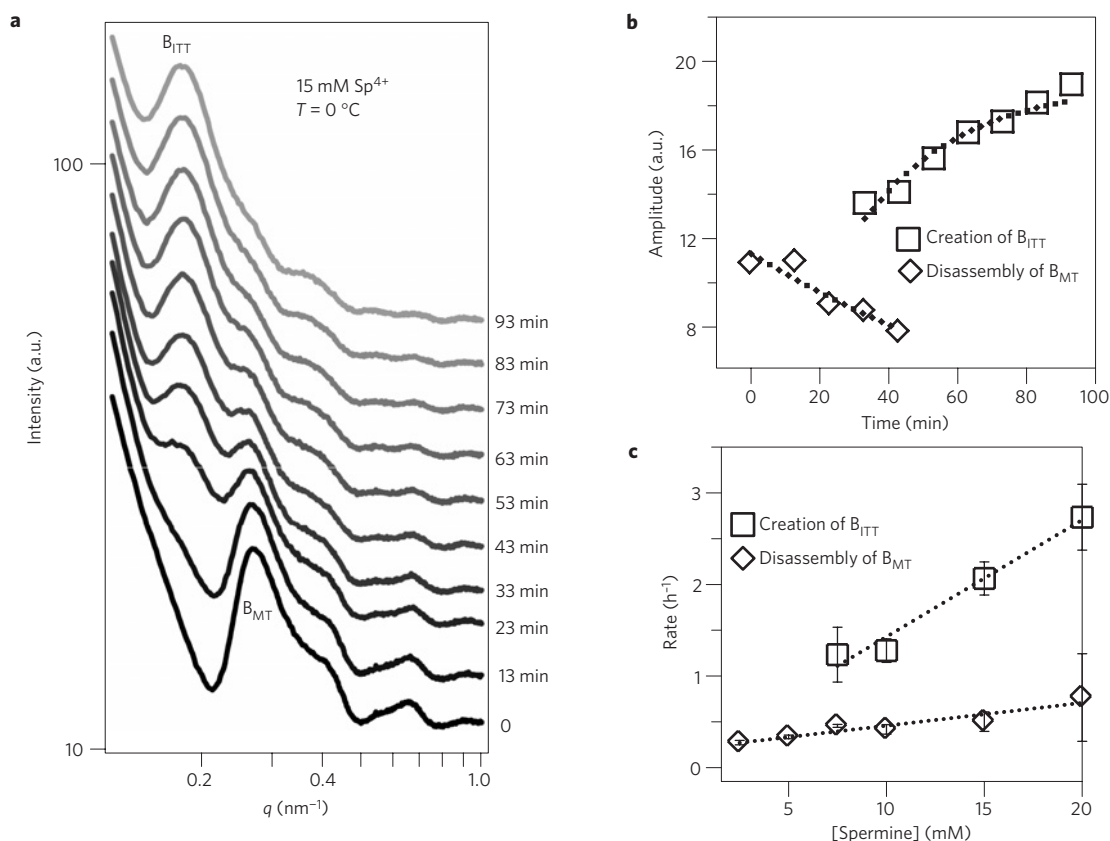
Figure 6 | Time-dependent synchrotron SAXS data of the transition kinetics from bundles of MTs (B$_{MT}$) to bundles of ITTs (B$_{ITT}$). a, The B$_{MT}$ phase was suddenly taken from room temperature to ≈0°C, and the resulting transition to the B$_{ITT}$ phase was followed in real time (t) by synchrotron SAXS. The profiles are for SAXS scans of a sample with 15 mM spermine taken at the temperature change ($t = 0$), 13 min after the temperature change, and subsequently every 10 min. The scans are offset for clarity. **b**, The amplitude of the (10) peak of the B$_{MT}$ phase (open diamonds) and the B$_{ITT}$ phase (open squares) obtained from best fits for the data in **a**. For simplicity, the (10) peaks of the coexisting B$_{MT}$ and B$_{ITT}$ phases were fitted to Gaussians. **c**, Rates of disassembly of the B$_{MT}$ phase ($R(B_{MT})$, open diamond) and creation of the B$_{ITT}$ phase ($R(B_{ITT})$, open squares) as a function of spermine concentration obtained from fits to SAXS data (as in **a,b** for 15 mM spermine). All SAXS samples were at a taxol/tubulin molar ratio of 0.55.

defining the discrete layer lines $q_z = 2\pi n/P$ for an infinite helix[37]. The second Gaussian term in equation (1) takes into account the finite cross-sectional size of the helical tubulin (that is, the thickness of tubulin). Here, R_g is the radius of gyration of the cross-section of the helical tubulin[38].

The B$_{ITT}$ SAXS data are dominated by the $n = 0$ line for the lower q data (<1 nm^{-1}) and the $n = 1$ line for the higher q data (>1 nm^{-1}). Fits of the data over the entire q range to the model (Fig. 5b, top profile, solid curve) gave a centre-to-centre distance of 45.6 nm for the inverted tubules. The bundle width inversely proportional to the width of the peaks was $L \approx 2(\pi \ln 4)^{0.5}/\kappa = 261$ nm, which corresponds to an average of 5.7 helices. The fit also gave $R = 20.2$ nm for the radius of the helical PFs (that is, obtained from the zeros of $J_0(q_\perp R)$), which is consistent with the TEM of ITTs (Figs 2b–d and 3j)).

The helical character of the tubulin oligomers, comprising the wall of the ITT seen in TEM (Figs 2b–d and 3j), is established unambiguously by the high quality of the fit of the model to the data in the higher q range (1.15 nm^{-1} < q < 1.4 nm^{-1}), where the helical form factor $|F_{\text{finite size helix}}|^2$ is now dominated by the $n = 1$ term (Fig. 5c; data are open circles; solid line is the fit to the helical model). The peak positions in the scattering data correspond precisely to the $n = 1$ layer Bessel function $J_1(q_\perp R)$, and gave a pitch of 5.29 nm with $R = 20.2$ nm. The best fit also yielded a physical radius of the tubulin cross-section (that is, the thickness of tubulin)[38], $R_{\text{tubulin}} = \sqrt{2}R_g \approx 2.12$ nm, close to electron microscopy data (≈2.5 nm) on tubulin[13], and an average helix

height $L_z \approx 317$ nm ($\propto$ inverse width of the high q peaks of Fig. 5c). If we fixed R_g at 1.77 (that is, $R_{\text{tubulin}} = 2.5$ nm), the quality of the fit was only slightly inferior, indicating that R_{tubulin} could not be determined better than ±0.2 nm.

We compared this helical model to a model of stacked rings of PFs, which gave a poor fit. For this latter model, a 1D structure factor along the stacking direction $S(q_z) = A\exp[(q_z - 2\pi/d)^2 L_z^2/4\pi]$ was multiplied by $|F_{\text{Ring}}|^2 \propto |[\sin(q_z T/2)/q_\perp q_z][(R_{\text{in}} + w)J_1 (q_\perp(R_{\text{in}} + w)) - R_{\text{in}}J_1(q_\perp R_{\text{in}})]|^2$, and orientationally averaged[38]. Here, F_{Ring} is the form factor of a ring with inner radius R_{in}, thickness T (that is, along the stacking direction) and width w. The dotted line in Fig. 5c, which is not able to predict the correct peak positions, is the best fit of the data to the stacked-ring model (with $d = 5.29$ nm, $T = 5.0$ nm, $w = 4.9$ nm, $R_{\text{in}} = 17.7$ nm (consistent with $R = R_{\text{in}} + w/2 = 20.2$ nm determined by the minima in the low q data), and $L_z =$ height of stacked rings of 343 nm). The chiral columnar nature of the B$_{ITT}$ phase makes it closely analogous to the chiral discotic phases of thermotropic liquid crystals[39,40].

To gain further insight into the nature of this phase change driven by a conformational change in the tubulin subunit, we have quantitatively characterized the kinetics of the B$_{MT}$-to-B$_{ITT}$ transition. Samples in the B$_{MT}$ phase were rapidly cooled to ≈0 °C (in an X-ray sample holder in thermal contact with a water bath), and SAXS was used to follow their evolution over short timescales of order 1–2 h (Fig. 6a). The gradual transformation of the B$_{MT}$ phase to the B$_{ITT}$ phase shows that there are significant energy barriers separating these phases. Assuming the bundle diameter within a

given phase does not significantly change, the amplitude of each peak is proportional to the number of bundles in that phase[41]. The (10) peak amplitudes are plotted as a function of time, t, in Fig. 6b, and fitted to a simple model of the transition kinetics. The destruction of the B_{MT} phase was fitted to a model assuming a constant rate of disassembly, $R(B_{MT})$. Thus, the amplitude of the (10) peak of the B_{MT} phase was assumed to be proportional to $\exp(-R(B_{MT})t)$. The amplitude of the (10) peak of the B_{ITT} phase was fitted to a function proportional to $\{1 - \exp[-R(B_{ITT})t]\}$, with $R(B_{ITT})$ being the constant rate of assembly of the B_{ITT} phase. If the B_{MT} phase decayed directly into the B_{ITT} phase, then $R(B_{ITT}) = R(B_{MT})$; otherwise they are not equal. For example, for 15 mM spermine (Fig. 6a), fits to the data gave $R(B_{MT}) = 0.5 \pm 0.1\,h^{-1}$ and $R(B_{ITT}) = 2.0 \pm 0.2\,h^{-1}$, indicating that there is at least one intermediate state between the two phases. As described earlier, TEM micrographs of samples transitioning from the B_{MT} to the B_{ITT} phase show that the B_{MT} phase disassembles into inside-out curling PFs with PF-rings self-assembling (in the presence of spermine) into the B_{ITT} phase. Thus, the transition between the two condensed phases occurs through a non-tubular intermediate.

The transformation of the B_{MT} phase, first to curved oligomers, and then to the B_{ITT} phase, involves overcoming two energy barriers with corresponding timescales $1/R(B_{MT})$ and $1/R(B_{ITT})$. The rate-limiting step in the disassembly of the B_{MT} phase to curved tubulin oligomers in the presence of spermine is presumably the rupture of the inter-PF bonds[12], and the kinetic barrier for the conversion of tubulin oligomers to helical columns may be due to the electrostatic repulsion between anionic oligomers (which is counteracted by cationic spermine). We have measured $R(B_{ITT})$ and $R(B_{MT})$ as a function of spermine concentration with SAXS (Fig. 6c), and found that the rates increase with spermine concentration. This finding establishes that spermine concentration modulates the barrier height between the straight and curved conformations of taxol-stabilized PFs, because the rate of disassembly, $R(B_{MT})$, which increases with spermine concentration, is proportional to $\exp(-\Delta E/k_B T)$, where ΔE is the energy barrier and k_B is the Boltzmann constant. It further suggests that spermine enhances the association of c-PFs into helices.

We note that the disassembly of taxol-stabilized MTs in the B_{MT} phase, due to lowering of the straight-to-curved energy barrier, is specific and occurs with spermine and not with spermidine or oligolysine on the timescales of two to three weeks studied in this paper (even at T of about a few degrees Celsius, where spermine disassembles the B_{MT} phase in hours). However, the assembly of tubulin rings (that is, GDP–tubulin in the absence of taxol and GTP) into the B_{ITT} phase is nonspecific and also occurs with oligolysine (5+) and spermidine (3+; see Supplementary Fig. 3).

This work shows that spermine controls the straight-to-curved transition rate in taxol-stabilized GDP–PFs. This has led to the creation of MT bundles, which on a spermine trigger undergo a dynamical transformation to an assembly of ITTs. The creation of such robust assemblies where the 'inner lumen' of MTs is stably exposed allows for a convenient platform for future experiments addressing interactions of biomolecules with the inner surface of MTs. Important examples of such molecules include the MT-associated protein tau (implicated in certain neurodegenerative diseases[42–44]), which has been hypothesized to have a MT inner lumen binding site (in addition to binding sites on the outer surface of MTs)[45,46], and cancer chemotherapy drugs targeting the MT inner lumen[16–19]. More generally, this work opens the path for a new paradigm for nanoscale assembly, which incorporates biological building blocks with a 'pre-programmed and triggerable' shape-evolving property. Owing to their inherent encoded properties, many enzymes (similar to tubulin GTPase employed in this work) would provide natural choices for building blocks of assemblies, which would disassemble on demand and reassemble the shape-remodelled building blocks into a different structure with distinct function. Applications may include encapsulation of molecules in the initial structure, and release on triggered disassembly.

Methods

Sample preparation. Purified tubulin was obtained from MAP-rich bovine brain MT protein as described previously[47]. MTs were polymerized from tubulin at $4\,mg\,ml^{-1}$ in 50 mM PIPES, at pH 6.8, 1 mM MgCl₂, 1 mM EGTA, 1 mM GTP and 5% glycerol by incubating in a 37 °C water bath for 20 min. The MTs were then stabilized by the addition of 20 µM taxol. The taxol-stabilized MTs were then sedimented through a sucrose cushion (to remove unpolymerized tubulin) and resuspended (to $4\,mg\,ml^{-1}$ tubulin) with 20 µM taxol–PEM₅₀ buffer. The final concentration for all TEM samples was $2\,mg\,ml^{-1}$ tubulin and 10 µM taxol (taxol/tubulin molar ratio of 0.55) after dilution by half by mixing equal volumes of MT and spermine (prepared using Millipore H₂O (18.2 MΩ)). Just before TEM was performed, the samples were diluted to $0.2\,mg\,ml^{-1}$ at the desired spermine concentration and immediately imaged. We also checked selected TEM samples where the sucrose cushion step (that is, to remove unpolymerized tubulin) was not performed. For these samples, TEM images depicting the early-stage outward curling of PFs leading to MT depolymerization are unchanged (compare Fig. 3a,d with 3b,c). However, in addition to the new ITTs described in the paper, we also observe co-existence with double-walled tubule structures (see Supplementary Fig. 4). These double-walled structures are not observed when the sucrose cushion step is employed. Previous studies have reported on similar double-walled structures obtained along a different pathway in mixtures of tubulin and cationic macromolecules[27–30].

Samples for TEM experiments were prepared as follows. Highly stable Formvar carbon-coated copper grids (Ted Pella) were loaded with sample, the excess solution was wicked off with Whatmann paper, 1 wt% uranyl acetate was added for 20 s, wicked off, and then washed with five drops of Millipore H₂O (18.2 MΩ). Unless otherwise noted, the samples were allowed to dry overnight before measurements. The X-ray samples were prepared by centrifuging the $2\,mg\,ml^{-1}$ tubulin and 10 µM taxol preparations (with the various concentrations of spermine as noted in the text) at 16,000g for 1 h. The pellets and supernatants were transferred to 1.5 mm quartz capillaries and sealed with a flame. The taxol-stabilized MTs used in the X-ray studies employed the sucrose cushion step to remove unpolymerized tubulin.

X-ray scattering. SAXS experiments were performed at beamline 4–2 of the Stanford Synchrotron Radiation Laboratory at 8.98 keV. Data analysis was done by incorporating the structure factors and form factors described in the text into widely available nonlinear least-squares fitting routines, and independently in program X+ (refs 48,49). The background subtracted from the raw SAXS data consisted of a polynomial that passed through the scattering minima of the SAXS data[21,22,34,35]. The widths of the bundles in the B_{MT} and B_{ITT} phases were determined by matching the Lorentzian squared structure factor ($[A_{hk}/(\kappa^2 + (q_\perp - G_{hk})^2)]^2$) at $|q_\perp - G_{hk}| = \kappa$ (with intensity at 1/4 of the maximum) to a Warren-type Gaussian line shape proportional to $\exp(-|q_\perp - G_{hk}|^2 L^2/4\pi)$ describing a lattice with domain size L (also with intensity at 1/4 of the maximum)[37]. This procedure leads to an average bundle width $L \approx 2(\pi \ln 4)^{0.5}/\kappa = 4.17/\kappa$. Alternatively, one may obtain the proportionality between L and $1/\kappa$ (which is proportional to the bundle width) by independently fitting the data either to a Lorentzian squared or a Warren-type Gaussian (which does not fit as well as a Lorentzian squared), and directly comparing L and $1/\kappa$. This procedure yields $L \approx 3.8/\kappa$ (which is within 10% of the former procedure).

Electron microscopy. Transmission experiments were performed at 80 kV in a JEM 1230 (JEOL) instrument at the University of California at Santa Barbara (Figs 2a–c and 4a–c, and Supplementary Fig. 2) and at 300 kV in a JEM-3011HR (JEOL) electron microscope in the National Nanofab Center at KAIST (Figs 2d and 3, Supplementary Figs 1 and 4).

References

1. Bray, D. *Cell Movements: From Molecules to Motility* 2nd edn (Garland, 2001).
2. Thomas, T. D., Earnshaw, W. C. & Lippincott-Schwartz, J. *Cell Biology* 2nd edn (Saunders, Elsevier, 2008).
3. Israelachvili, J. N. *Intermolecular & Surface Forces* (Academic, 1992).
4. Sackmann, E. Membrane bending energy concept of vesicle-shape and cell-shape and shape-transitions. *FEBS Lett.* **346,** 3–16 (1994).
5. Chiruvolu, S. *et al.* A phase of liposomes with entangled tubular vesicles. *Science* **266,** 1222–1225 (1994).

6. Zidovska, A. *et al.* Block liposomes from curvature-stabilizing lipids: Connected nanotubes, -rods and -spheres. *Langmuir* **25,** 2979–2985 (2009).
7. Zidovska, A. *et al.* Block liposome and nanotube formation is a general phenomenon of membranes containing multivalent lipids. *Soft Matter* **7,** 8363–8369 (2011).
8. Seeman, N. C. & Belcher, A. M. Emulating biology: Building nanostructures from the bottom up. *Proc. Natl Acad. Sci. USA* **99,** 6451–6455 (2002).
9. Ringler, P. & Schulz, G. E. Self-assembly of proteins into designed networks. *Science* **302,** 106–109 (2003).
10. Seeman, N. C. DNA in a material world. *Nature* **421,** 427–431 (2003).
11. Chworos, A. *et al.* Building programmable jigsaw puzzles with RNA. *Science* **306,** 2068–2072 (2004).
12. Nogales, E., Wang, H. W. & Niederstrasser, H. Tubulin rings: Which way do they curve. *Curr. Opin. Struct. Biol.* **13,** 256–261 (2003).
13. Lowe, J., Li, H., Downing, K. H. & Nogales, E. Refined structure of alpha beta-tubulin at 3.5 Å resolution. *J. Mol. Biol.* **313,** 1045–1057 (2001).
14. Ravelli, R. B. G. *et al.* Insight into tubulin regulation from a complex with colchicine and a stathmin-like domain. *Nature* **428,** 198–202 (2004).
15. Mandelkow, E. M., Mandelkow, E. & Milligan, R. A. Microtubule dynamics and microtubule caps: A time-resolved cryo-electron microscopy study. *J. Cell Biol.* **114,** 977–991 (1991).
16. Nogales, E., Wolf, S. G., Khan, I. A., Luduena, R. F. & Downing, K. H. Structure of tubulin at 6.5 Å and location of the taxol-binding site. *Nature* **375,** 424–427 (1995).
17. Mitra, A. & Sept, D. Taxol allosterically alters the dynamics of the tubulin dimer and increases the flexibility of microtubules. *Biophys. J.* **95,** 3252–3258 (2008).
18. Jordan, M. A. & Wilson, L. Microtubules as a target for anticancer drugs. *Nature Rev. Cancer* **4,** 253–265 (2004).
19. Jordan, M. A. & Wilson, L. in *Cancer Drug Discovery and Development, The Role of Microtubules in Cell Biology, Neurobiology, and Oncology* (ed. Fojo, T.) 47–81 (Humana Press, 2008).
20. Elie-Caille, C. *et al.* Straight GDP-tubulin protofilaments form in the presence of taxol. *Curr. Biol.* **17,** 1765–1770 (2007).
21. Choi, M.C. *et al.* Human microtubule-associated-protein tau regulates the number of protofilaments in microtubules: A synchrotron X-ray scattering study. *Biophys. J.* **97,** 519–527 (2009).
22. Needleman, D. J. *et al.* Higher-order assembly of microtubules by counterions: From hexagonal bundles to living necklaces. *Proc. Natl. Acad. Sci. USA* **101,** 16099–16103 (2004).
23. Gelbart, W. M., Bruinsma, R. F., Pincus, P. A. & Parsegian, V. A. DNA-inspired electrostatics. *Phys. Today* **53,** 38–44 (2000).
24. Koltover, I., Wagner, K. & Safinya, C. R. DNA condensation in two dimensions. *Proc. Natl Acad. Sci. USA* **97,** 14046–14051 (2000).
25. Manning, G. S. Limiting laws and counterion condensation in polyelectrolyte solutions I. Colligative properties. *J. Chem. Phys.* **51,** 924–933 (1969).
26. Savarin, P. *et al.* Central role for polyamines in microtubule assembly in cells. *Biochem. J.* **430,** 151–159 (2010).
27. Jacobs, M., Bennett, P. M. & Dickens, M. J. Duplex microtubule is a new form of tubulin assembly induced by polycations. *Nature* **257,** 707–709 (1975).
28. Erickson, H. P. & Voter, W. A. Polycation-induced assembly of purified tubulin. *Proc. Natl. Acad. Sci. USA* **73,** 2813–2817 (1976).
29. Kuznetsov, S. A., Gelfand, V. I., Rodionov, V. A., Rosenblat, V. A. & Gulyaeva, J. G. Polymerization of purified tubulin by synthetic polycations. *FEBS Lett.* **95,** 343–346 (1978).
30. Erickson, H. P. in *Cell Motility* (eds Goldman, R., Pollard, T. & Rosenbaum, J.) (Cold Spring Harbor, 1976).
31. Howard, W. D. & Timasheff, S. N. GDP state of tubulin: Stabilization of double rings. *Biochemistry* **25,** 8292–8300 (1986).
32. Nicholson, W. V., Lee, M., Downing, K. H. & Nogales, E. Cryo-electron microscopy of GDP-tubulin rings. *Cell Biochem. Biophys.* **31,** 175–183 (1999).
33. Wang, H-W. & Nogales, E. Nucleotide-dependent bending flexibility of tubulin regulates microtubule assembly. *Nature* **435,** 911–915 (2005).
34. Raviv, U. *et al.* Cationic liposome-microtubule complexes: Pathways to the formation of two-state lipid-protein nanotubes with open or closed ends. *Proc. Natl Acad. Sci. USA* **102,** 11167–11172 (2005).
35. Raviv, U. *et al.* Microtubule protofilament number is modulated in a stepwise fashion by the charge density of an enveloping layer. *Biophys. J.* **92,** 278–287 (2007).
36. Cochran, W., Crick, F. H. C. & Vand, V. The structure of synthetic polypeptides. I. The transform of atoms on a helix. *Acta Crystal.* **5,** 581–586 (1952).
37. Warren, B. E. X-ray diffraction in random layer lattice. *Phys. Rev.* **59,** 693–698 (1941).
38. Glatter, O. & Kratky, O. (eds) in *Small Angle X-ray Scattering* 155–156 (Academic, 1982).
39. Levelut, A. Structure of a disk-like mesophase. *J. Physique* **40,** 8184–8188 (1979).
40. Safinya, C. R., Liang, K. S., Varady, W. A., Clark, N. A. & Andersson, G. Synchrotron X-ray study of the orientational ordering D2-D1 structural phase transition of freely suspended discotic strands in triphenylene-hexa-dodecanoate. *Phys. Rev. Lett.* **53,** 1172–1175 (1984).
41. Guinier, A. *X-Ray Diffraction in Crystals, Imperfect Crystals, and Amorphous Bodies* (Dover, 1963).
42. Goedert, M. & Spillantini, M. G. A century of Alzheimer's disease. *Science* **314,** 777–781 (2006).
43. Roberson, E. D. & Mucke, L. 100 Years and counting: Prospects for defeating Alzheimer's disease. *Science* **314,** 781–784 (2006).
44. Morris, M., Maeda, S., Vossel, K. & Mucke, L. The many faces of tau. *Neuron* **70,** 410–426 (2011).
45. Kar, S., Fan, J., Smith, M. J., Goedert, M. & Amos, L. A. Repeat motifs of tau bind to the insides of microtubules in the absence of taxol. *EMBO J.* **22,** 70–77 (2003).
46. Makrides, V., Massie, M. R., Feinstein, S. C. & Lew, J. Evidence for two distinct binding sites for tau on microtubules. *Proc. Natl Acad. Sci. USA* **101,** 6746–6751 (2004).
47. Miller, H. P. & Wilson, L. Preparation of microtubule protein and purified tubulin from bovine brain by cycles of assembly and disassembly and phosphocellulose chromatography. *Methods Cell Biol.* **95,** 2–15 (2010).
48. Szekely, P., Ginsburg, A., Ben Nun, T. & Raviv, U. Solution X-ray scattering form factors of supramolecular self-assembled structures. *Langmuir* **26,** 13110–13129 (2010).
49. Ben Nun, T., Ginsburg, A., Szekely, P. & Raviv, U. X+: A comprehensive, computationally accelerated, structural analysis tool of solution X-ray scattering from supramolecular self-assemblies. *J. Appl. Crystallogr.* **43,** 1522–1531 (2010).

Author contributions

M.A.O-L., C.S. and M.C.C. performed electron microscopy, and M.A.O-L. and D.J.N. took X-ray data. H.P.M. purified tubulin. C.R.S., D.J.N., Y.L., U.R. and M.A.O-L. developed X-ray structure and form factors, and D.J.N. and A.G. carried out X-ray line-shape analysis. Y.L. and P.A.K. performed the statistical analysis of ring diameters, and Y.L. wrote the Supplementary Information. C.R.S., D.J.N. and M.A.O-L. wrote the paper. M.C.C., C.S., Y.L., U.R., H.P.M. and L.W. engaged in discussions and critical comments on the manuscript.

Additional information

Supplementary information is available in the online version of the paper. Reprints and permissions information is available online at www.nature.com/reprints. Correspondence and requests for materials should be addressed to C.R.S.

Competing financial interests

The authors declare no competing financial interests.